Remote Sensing in Hybridized Arrays of Nanostrings

T. S. Biswas,[†,§] Jin Xu,[†,§] X. Rojas,[†] C. Doolin,[†] A. Suhel,[†] K. S. D. Beach,*,[†,‡] and J. P. Davis*,[†]

[†]Department of Physics, University of Alberta, Edmonton, Alberta Canada T6G 2E1

[‡]Department of Physics and Astronomy, The University of Mississippi, University, Mississippi 38677, United States

S Supporting Information

ABSTRACT: We study high-Q nanostrings that are joined end-to-end to form coupled linear arrays. Whereas isolated individual resonators exhibit sinusoidal vibrational modes with an almost perfectly harmonic spectrum, the modes of the interacting strings are substantially hybridized. Even far-separated strings can show significantly correlated displacement. This remote coupling property is exploited to quantify the deposition of femtogram-scale masses with string-by-string positional discrimination based on measurements of one string only.

KEYWORDS: Silicon nitride nanostrings, coupled arrays, hybridization, remote detection, parallel mass sensing
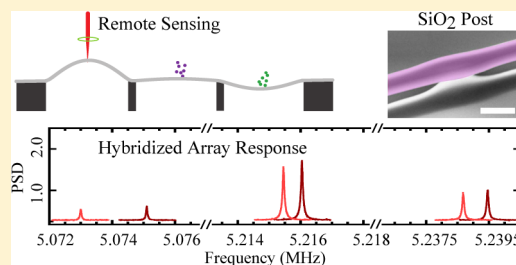
Fantastic progress has been made in the use of individual nanomechanical resonators for atomic and molecular sensing.[1−8] Yet the most striking potential of nanomechanics lies in the use of arrays[9] of resonators to detect multiple molecular species simultaneously,[10] thus performing parallel molecular analysis.[11−13] In certain geometries, these resonators can become coupled to form hybridized arrays,[14,15] offering new capabilities as a result. Here we present the first example of strongly coupled silicon nitride (Si₃N₄) nanostrings[16−21] arranged in a one-dimensional (1D) array. As a result of mode hybridization, we can detect the state of all resonators in the array from measurements performed on a single one (as anticipated in ref 22.). The ability to extract information while focusing on just one string greatly simplifies our optical interferometric measurement system and has the potential to streamline other methods of detection as well.[11] The analysis relies on numerical techniques that we have developed to rapidly characterize the system's response to mass added anywhere in the array. We have successfully carried out single-blind comparisons between the theoretical predictions and experimental mass deposition.

Previous studies of mutually interacting nanomechanical resonators have typically employed cantilevers[14,15] or doubly clamped beams[23,24] that are weakly coupled through a mutual overhang. Instead, we have developed 1D arrays of stringlike resonators, fabricated from a contiguous strip of silicon nitride under high intrinsic tension with the individual resonators defined by the placement of small support posts (Figure 1A). A device design with posts on the micrometer scale (Figure 1C) leads to strong hybridization and a substantial frequency splitting between modes that are delocalized across the entire array. As a result, remote sensing and characterization are possible. We use silicon nitride nanostrings because their mechanical quality factors are exceptionally high[18−20,25−27] and because their sinusoidal mode shapes encourage strong coupling through the posts.

The nanostrings are fabricated from stoichiometric silicon nitride (250 nm) deposited onto silicon dioxide (2 μm) on a silicon substrate (0.5 mm). Standard optical lithography is performed, followed by reactive ion etching of the silicon nitride. The device is released with a buffered oxide etch of the silicon dioxide that is timed to produce the desired size of the coupling posts. The complete arrays are then mounted inside an optically accessible vacuum chamber. The experimental data is collected using standard optical interferometry with a 632.8 nm laser focused to a ~1 μm diameter spot onto the nanostring, as described elsewhere.[20] The optical power incident on the nanostrings, ~200 μW, does not cause significant heating. The interferometric signal is amplified after detection and is analyzed using a high frequency lock-in amplifier (Zurich Instruments HF2LI). Driven data can be acquired using an external piezoelectric (see Figures S.1 and S.2 of the Supporting Information), which allows for phase-locked loop measurements (Supporting Information Figure S.4). For thermomechanical measurements, optimized time domain data is acquired within a bandwidth around the device frequency and then Fourier transformed. In this way, multiple data sets can be taken very quickly and averaged together for increased signal-to-noise, a key requirement for practical sensing applications.

The out-of-plane motion of these devices, $z(x,t)$, can be accurately represented by a Lagrangian $L = \int dx \, (\mu(x)(\partial_t z)^2 - U[z(x,t)])$ in which $\mu(x) = \rho A + 1/3\pi(x)\rho' A'$ is the linear mass density along the device and

$$U = \frac{\sigma A}{2}(\partial_x z)^2 + \frac{EI_y}{2}(\partial_x^2 z)^2 + \pi(x)\frac{E'a}{2h}z^2 \qquad (1)$$
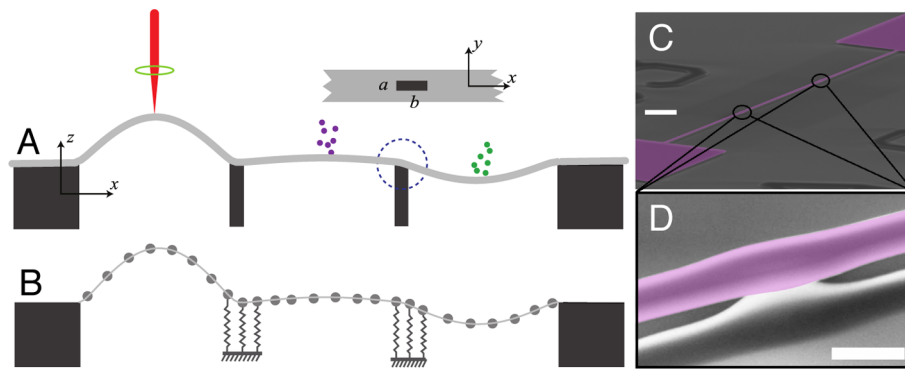
Figure 1. (A) Side-view schematic of the mode of next-to-lowest energy for an array of three nanostrings (with the out-of-plane motion highly exaggerated). A top view shows the $a \times b$ rectangular cross-section of one of the supporting posts. (B) Representation of the corresponding finite-difference modeling. (C) SEM image of the three-string device (angled from above). The scale bar represents a distance of 10 μm. (D) Magnified image of the silicon dioxide post with a 1 μm scale bar.

is a model of the potential energy that accounts for stretching and bending of the string and elongation of the posts. Here, ρ and E are the volumetric mass density and the Young's modulus for silicon nitride; A is the (yz plane) cross-sectional area of the string; and I_y is a bending moment of inertia (around the y-axis). The primed constants represent the corresponding quantities for the silicon dioxide post, and the geometric factor 1/3 that appears in $\mu(x)$ properly accounts for the post's kinetic energy under bulk deformation. The Lagrangian density is spatially discontinuous by virtue of a bump function $\pi(x)$ that takes the value one wherever there is a post and zero otherwise. Further details on the theoretical model can be found in the Supporting Information.

By way of conventional finite-difference techniques (see the schematic in Figure 1B), we are able to obtain numerical solutions that provide the mode shapes and natural frequencies of all the out-of-plane vibrational excitations. (The large width relative to thickness of the device, more strip than string, suppresses in-plane motion.) With some modest fine-tuning of the geometric parameters, we find that we are able to match the simulated modes to the measured ones with good accuracy.

Individual strings under high intrinsic tension have a close-to-harmonic spectrum with a large, nearly uniform spacing between modes. If we form an array from N strings that are roughly the same size, then we expect the hybridization to occur in bundles of N-like frequencies, each of which can be treated independently. The lowest bundle, formed from the coupled fundamental frequencies of the N individual resonators, can be described by a dynamical matrix having the following band diagonal form:

$$\begin{pmatrix} \dfrac{\kappa_1}{m_1} & \dfrac{t_{1,2}}{\sqrt{m_1 m_2}} & 0 & \cdots \\[2ex] \dfrac{t_{1,2}}{\sqrt{m_1 m_2}} & \dfrac{\kappa_2}{m_2} & \dfrac{t_{2,3}}{\sqrt{m_2 m_3}} & \\[2ex] 0 & \dfrac{t_{2,3}}{\sqrt{m_2 m_3}} & \ddots & \\[2ex] \vdots & & & \dfrac{\kappa_N}{m_N} \end{pmatrix} \quad (2)$$

The eigenvalue-eigenvector pairs (λ_n; $A_{n,j}$) give the square of the angular frequency, $\lambda_n = (2\pi f_n)^2$, and the deflection

amplitude on string segment j for each of modes $n = 1,2,...,N$. The trace property of eq 2 implies that $\Lambda_+ = \Sigma_{j=1}^{N} \lambda_j = \Sigma_{j=1}^{N} \kappa_j / m_j$, which is independent of the post couplings. Λ_+ is sensitive to the total (nonspecific) mass added to the device.

For a two-string array, there is a closed-form solution with

$$\lambda_{2,1} = \frac{1}{2}\left(\frac{\kappa_1}{m_1} + \frac{\kappa_2}{m_2} \pm \left[\left(\frac{\kappa_1}{m_1} - \frac{\kappa_2}{m_2} \right)^2 + \frac{4 t_{1,2}^2}{m_1 m_2} \right]^{1/2} \right)$$

$$(3)$$

and it is straightforward to linearize the expressions for λ_1 and λ_2 in terms of small mass increments. For longer arrays ($N > 2$), we simply diagonalize eq 2 and judge its response to mass perturbation with numerical derivatives. In either case, measurements of the N low-lying frequencies before and after mass deposition ($m_j \rightarrow m_j + \delta m_j$) can be inverted to determine unknown values of δm_j, provided that the dynamical matrix is known.

We can populate eq 2 in one of two ways. First, we can "downfold" the full numerical simulation, based on the Lagrangian preceding eq 1. Alternately, we can recognize that $N + (N - 1) = 2N - 1$ known quantities are needed to fix the diagonal and off-diagonal elements of the matrix. We obtain these by measuring the resonant frequencies f_n for $n = 1,2,...,N$ and the relative amplitudes $|A_{n,1}/A_{1,1}|$ for $n = 2,3, ..., N$, all carried out with interferometry performed on the first string. The dynamical matrix is then completely determined via the Lanczos algorithm (see ref 28 and references therein). The procedure just described serves as a characterization of the system that only needs to be carried out once, before any subsequent mass deposition.

On two- and three-string systems, we have performed experiments in which the initial dynamical matrix is determined and then additional mass at the femtogram level is selectively deposited on particular strings. The mass addition is accomplished by bombarding the center of the target string with a highly collimated electron beam from a scanning-electron microscope (SEM). The exposure is timed and calibrated to the relative frequency shift $\delta f_1/f_1 = -\delta m_1/m_1$ observed in a single-string reference device on the same chip. Here, m_1 is determined from the silicon nitride density $\rho = 3100$ kg/m^3 and the string volume, as estimated from high-resolution SEM images.

The two-string system offers the simplest possible test of our ability to predict shifts in the frequencies of the normal modes as a result of added mass. The data shown in Figure 2 are taken
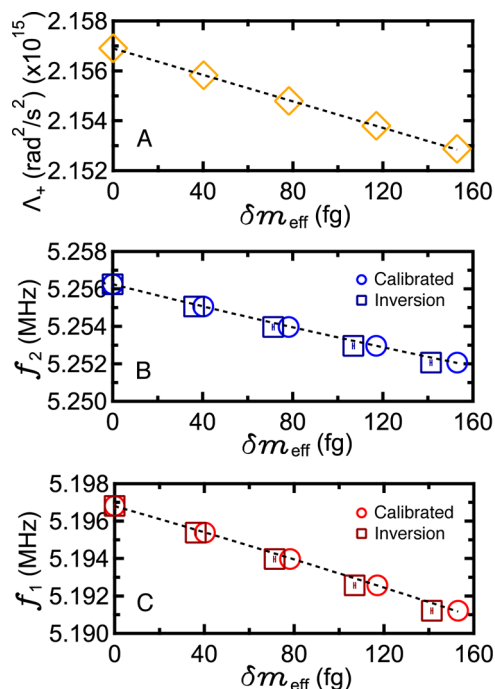

Figure 2. Data from a mass deposition experiment performed on a two-string array. (A) Λ_+ is the sum of the eigenvalues of the dynamical matrix. Measured values (yellow diamonds) are plotted alongside $\kappa_1/m_1 + (\kappa_2/m_2)(1 + \delta m_2/m_2)^{-1}$ (dashed line), the analytical expression for the predicted behavior. The total mass deposition inferred from Λ_+ and the SEM calibration agree. (B,C) Theory tells us that the mass accumulation should reveal itself as a downward shift of the frequencies of the lowest two vibrational modes. Frequencies f_1 and f_2 are observed to behave in exactly that way. The dashed lines show $(\lambda_1)^{1/2}/2\pi$ and $(\lambda_2)^{1/2}/2\pi$ from eq 3. The values $\kappa_1/m_1 = 1.07931(7)$, $\kappa_2/m_2 = 1.07759(7)$, and $t_{1,2}/(m_1 m_2)^{1/2} = 0.01224(1)$, expressed in units $\times 10^{15}\ \mathrm{s}^{-2}$, are taken from a simultaneous fit to the measured resonant frequencies. These compare well to the corresponding values, 1.07983(3), 1.07708(3), and 0.012186(3), obtained via Lanczos from the initial characterization measurements.

on a device $\approx 100\ \mu$m long. Observation and numerical simulation are in excellent agreement if we assume that the string is broken into two segments $L_1 = 50.55\ \mu$m, $L_2 = 50.65\ \mu$m by a single post with dimensions $a = 0.2\ \mu$m and $b = 1.0\ \mu$m (see Figure 1). The top panel of Figure 2 shows Λ_+ (determined from resonant frequencies measured on string 1); its negative slope is consistent with the mass accumulation inferred from the SEM process targeting string 2. The lower two panels show the theoretical and observed softening of the vibration modes. Also plotted are results from our inversion procedure in which the dynamical matrix is fixed from measurements of the frequencies and relative amplitudes, and the mass changes determined from the subsequent frequency shifts.

Our second test case is a three-string array, composed of segments of length $L_1 = 50.75\ \mu$m, $L_2 = 51.30\ \mu$m, and $L_3 = 50.55\ \mu$m. Figure 3 illustrates the characteristic rearrangement of resonances in response to ~40 fg of mass placed onto its third string. Fitting the peaks in the power spectral density[29] (PSD) provides the frequencies f_n and amplitudes $|A_{n,j}|$ of the
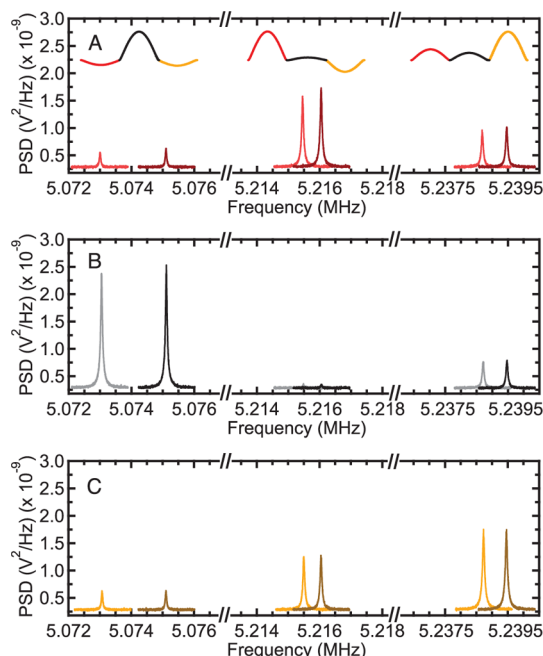

Figure 3. Thermomechanical resonances for the (A) first, (B) second, and (C) third strings in a three-string array. The three eigenmodes are measured on each string before (dark) and after (light) 40 fg has been deposited onto the third string. We observe that all resonances shift to lower values. The inset in (A) shows the simulated amplitude profiles for the three lowest modes in their initial state before mass deposition.

resonances, before and after deposition. The fitting form is a damped harmonic oscillator line shape superimposed on a flat noise background. (See the Supporting Information.)

It is worth noting that both the eigenvalues (proportional to the square of the peak frequencies in Figure 3) and the eigenvectors (the displacement amplitudes on each string) of the dynamical matrix are altered by the addition of mass to any single string. Because the fractional change in the amplitudes is many times larger than the corresponding change in the frequencies, it has been suggested, in the context of coupled cantilevers,[14] that amplitude measurements provide greater sensitivity to added mass. To the contrary, our careful study of the system's response in each of these channels (using the Allan deviation, see the Supporting Information) reveals that this is not the case, at least not for our coupled nanostring system. The mode amplitudes are subject to much higher background noise than the frequencies and therefore are unsuitable for mass sensing, except as part of the initial characterization step in which the $N - 1$ relative amplitudes play a role in fixing the elements of the dynamical matrix.

Figure 4 shows the evolution of the resonant frequencies as strings 3, 2, and 1 of the three-string system are targeted in turn for mass deposition with the SEM. Plotted alongside the experimental measurements are numerical predictions obtained from running our model forward (predicting frequency shifts from knowledge of the mass added) and backward (predicting mass added from the observed frequency shifts). Testing the forward technique is an important self-consistency check; it verifies that our analytical framework is expressive enough to describe the experimental reality and that we have good control over where mass is being added during the SEM process. The backward technique is the full inversion that would actually be performed in a real-world sensing device. It determines mass
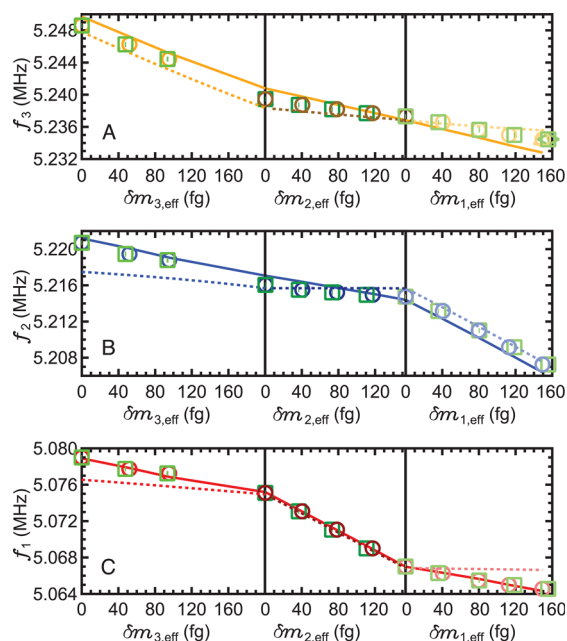
Figure 4. Mass is added to strings 3, 2, and 1 of a three-string array, cumulatively and in sequence. The frequencies of the strongly hybridized modes are plotted against the calibrated mass deposition (circles). Having first characterized the dynamical matrix from measurements of the initial frequencies and relative amplitudes, we use the inverse solver to map the frequency shifts into predictions for the mass added to each particular string (squares). These two data sets were obtained independently from one other. The dashed line is the forward prediction of the model with the calibrated δm as input. The solid line represents a theoretical best fit to the $(\delta m, f)$ data in which the dynamical system matrix has been determined variationally along with one free parameter that represents the amount of extra mass accruing to the nontargeted strings during each SEM session.

additions from frequency shifts and could be easily integrated into an experimental data acquisition system to provide seamless real-time calibrated mass sensing.

We have shown that strongly coupled silicon nitride nanostrings, organized into 1D arrays, offer a compelling platform for parallelized sensing applications. The hybridized normal modes can be accurately simulated using a finite-difference solver. When mass is deposited on any one string, the frequencies of all the modes respond in a characteristic way. These small frequency shifts can be measured remotely, on a single "sensing" string. Most importantly, once the system's pre-mass-deposition dynamical matrix is determined from the mode frequencies and relative amplitudes, as measured on a single string, an inverse solver can be used to transform the frequency shifts, again measured on a single string, into inferred values for the mass added to each string in the array. The results of this inversion technique have been compared to the calibrated mass deposition values with excellent agreement. We have demonstrated remote sensing capability in both two- and three-string arrays, and there is no practical impediment to extending this work to larger arrays, or even to collections of coupled resonators in two dimensions.[30−33]

■ ASSOCIATED CONTENT

Ⓢ Supporting Information

Details of the system modeling and inversion algorithm; experimental determination of the maximum mass sensitivity from measurements of the Allan deviation. This material is available free of charge via the Internet at http://pubs.acs.org.

■ AUTHOR INFORMATION

Corresponding Authors

*E-mail: (K.S.D.B.) kbeach@ualberta.ca.
*E-mail: (J.P.D.) jdavis@ualberta.ca.

Author Contributions

§T.S.B. and J.X. contributed equally.

Notes

The authors declare no competing financial interest.

■ REFERENCES

(1) Jensenius, H.; Thaysen, J.; Rasmussen, A. A.; Veje, L. H.; Hansen, O.; Boisen, A. *Appl. Phys. Lett.* **2000**, *76*, 2615.
(2) Dohn, S.; Sandberg, R.; Svendsen, W.; Boisen, A. *Appl. Phys. Lett.* **2005**, *86*, 233501.
(3) Chiu, H.-Y.; Hung, P.; Postma, H. W. Ch.; Bockrath, M. *Nano Lett.* **2008**, *8*, 4342.
(4) Yi, D.; Greve, A.; Hales, J. H.; Senesac, L. R.; Davis, Z. J.; Nicholson, D. M.; Boisen, A.; Thundat, T. *Appl. Phys. Lett.* **2008**, *93*, 154102.
(5) Naik, A. K.; Hanay, M. S.; Hiebert, W. K.; Feng, X. L.; Roukes, M. L. *Nat. Nanotechnol.* **2009**, *4*, 445.
(6) Godin, M.; Tabard-Cossa, V.; Miyahara, Y.; Monga, T.; Williams, P. J.; Beaulieu, L. Y.; Lennox, R. B.; Grutter, P. *Nanotechnology* **2010**, *21*, 075501.
(7) Arlett, J. L.; Myers, E. B.; Roukes, M. L. *Nat. Nanotechnol.* **2001**, *6*, 203.
(8) Hanay, M. S.; Kelber, S.; Naik, A. K.; Chi, D.; Hentz, S.; Bullard, E. C.; Colinet, E.; Duraffourg, L.; Roukes, M. L. *Nat. Nanotechnol.* **2012**, *7*, 602.
(9) Buks, E.; Roukes, M. L. *J. Microelectromech. Syst.* **2002**, *11*, 802−807.
(10) Yoo, Y. K.; Chae, M.-S.; Kang, J. Y.; Kim, T. S.; Hwang, K. S.; Lee, J. H. *Anal. Chem.* **2012**, *84*, 8240.
(11) Li, M.; Myers, E. B.; Tang, H. X.; Aldridge, S. J.; McCaig, H. C.; Whiting, J. J.; Simonson, R. J.; Lewis, N. S.; Roukes, M. L. *Nano Lett.* **2010**, *10*, 389.
(12) Sampathkumar, A.; Ekinci, K. L.; Murrays, T. W. *Nano Lett.* **2011**, *11*, 1014.
(13) Bargatin, I.; Myers, E. B.; Aldridge, J. S.; Marcoux, C.; Brianceau, P.; Duraffourg, L.; Colinet, E.; Hentz, S.; Andreucci, P.; Roukes, M. L. *Nano Lett.* **2012**, *12*, 1269.
(14) Gil-Santos, E.; Ramos, D.; Jana, A.; Calleja, M.; Raman, A.; Tamayo, J. *Nano Lett.* **2009**, *9*, 4122.
(15) Gil-Santos, E.; Ramos, D.; Pini, V.; Calleja, M.; Tamayo, J. *Appl. Phys. Lett.* **2011**, *98*, 123108.
(16) Unterreithmeier, Q. P.; Weig, E. M.; Kotthaus, J. P. *Nature* **2009**, *458*, 1001.
(17) Anetsberger, G.; Arcizet, O.; Unterreithmeier, Q. P.; Riviére, R.; Schliesser, A.; Weig, E. M.; Kotthaus, J. P.; Kippenberg, T. J. *Nat. Phys.* **2009**, *5*, 909−914.
(18) Verbridge, S. S.; Parpia, J. M.; Reichenbach, R. B.; Bellan, L. M.; Craighead, H. G. *J. Appl. Phys.* **2006**, *99*, 124304.
(19) Schmid, S.; Jensen, K. D.; Nielsen, K. H.; Boisen, A. *Phys. Rev. B* **2011**, *84*, 165307.
(20) Suhel, A.; Hauer, B. D.; Biswas, T. S.; Beach, K. S. D.; Davis, J. P. *Appl. Phys. Lett.* **2012**, *100*, 173111.

(21) Defoort, M.; Lulla, K. J.; Blanc, C.; Ftouni, H.; Bourgeois, O.; Collin, E. *J. Low Temp. Phys.* **2013**, *171*, 731−736.

(22) Choubey, B.; Anthony, C.; Saad, N. H.; Ward, M.; Turnbull, R.; Collins, S. *Appl. Phys. Lett.* **2010**, *97*, 133114.

(23) Karabalin, R. B.; Cross, M. C.; Roukes, M. L. *Phys. Rev. B* **2009**, *79*, 165309.

(24) Okamoto, H.; Kamada, T.; Onomitsu, K.; Mahboob, I.; Yamaguchi, H. *Appl. Phys. Expr.* **2009**, *2*, 062202.

(25) Lee, S.; Adiga, V. P.; Barton, R. A.; van der Zande, A. M.; Lee, G.-H.; Ilic, B. R.; Gondarenko, A.; Parpia, J. M.; Craighead, H. G.; Hone, J. *Nano Lett.* **2013**, *13*, 4275−4279.

(26) Southworth, D. R.; Barton, R. A.; Verbridge, S. S.; Ilic, B. R.; Fefferman, A. D.; Craighead, H. G.; Parpia, J. M. *Phys. Rev. Lett.* **2009**, *102*, 225503.

(27) Sankey, J. C.; Yang, C.; Zwickl, B. M.; Jayich, A. M.; Harris, J. G. E. *Nat. Phys.* **2010**, *6*, 707.

(28) Gladwell, G. M. L. Inverse Problems in Vibration. In *Solid Mechanics and Its Applications*, 2nd ed.;Springer: New York, 2004; Vol. *119*.

(29) Hauer, B. D.; Doolin, C.; Beach, K. S. D.; Davis, J. P. *Ann. Phys.* **2013**, *339*, 181.

(30) Judgea, J. A.; Houston, B. H.; Photiadis, D. M.; Herdic, P. C. *J. Sound Vib.* **2006**, *290*, 1119−1140.

(31) Zalalutdinova, M. K.; Baldwin, J. W.; Marcus, M. H.; Reichenbach, R. B.; Parpia, J. M.; Houston, B. H. *Appl. Phys. Lett.* **2006**, *88*, 143504.

(32) Kharrat, C.; Colinet, E.; Duraffourg, L.; Hentz, S.; Andreucci, P.; Voda, A. *IEEE Trans. Ultrason., Ferroelectr., Freq. Control* **2010**, *57* (6), 1285−1295.

(33) Mayer Alegre, T. P.; Safavi-Naeini, A.; Winger, M.; Painter, O. *Opt. Express* **2011**, *19*, 5658−5669.